Journal of
Materials Chemistry A

Materials for energy and sustainability

This article can be cited before page numbers have been issued, to do this please use: S. Agrotis, M. Lin, K. H. Mehta, O. S. J. Hagger, R. I. Made, I. P. Parkin, D. J. Caruana and A. D. Handoko, *J. Mater. Chem. A*, 2026, DOI: 10.1039/D6TA02615J.

View Article Online
DOI: 10.1039/D6TA02615J

Direct Atmospheric Pressure Plasma Jet (APPJ) Synthesis of Nanosized CuO_x-Ag Composites for Efficient Electrochemical CO_2 Reduction to Multi-Carbon Products

Stefanos Agrotis[1,2], Ming Lin[2], Kallum Hiten Mehta[1,2], Oliver S. J. Hagger[1], Riko I. Made[2], Ivan P. Parkin[1], Daren J. Caruana[1,*], and Albertus D. Handoko[3,*]

[1] Department of Chemistry, Christopher Ingold Laboratories, 20 Gordon St., WC1H 0AJ, London, United Kingdom. E-mail: d.j.caruana@ucl.ac.uk
*[2] Institute of Materials Research and Engineering (IMRE), Agency for Science, Technology and Research (A*STAR), 2 Fusionopolis Way, Innovis #08-03, Singapore 138634, Republic of Singapore.*
*[3] Institute of Sustainability for Chemicals, Energy and Environment ($ISCE^2$), Agency for Science, Technology and Research (A*STAR), 1 Pesek Road, Singapore 627833, Republic of Singapore. Email: Handoko_Albertus@a-star.edu.sg*

Abstract

Atmospheric pressure plasma jet (APPJ) is an emerging technique capable of synthesising ligand-free nanosized composites with controllable configuration ratio. Here, APPJ is used to synthesise and directly deposit CuO_x-Ag for electrocatalytic CO_2 reduction reaction (CO_2RR). The morphology of CuO_x-Ag composites evolves from Janus-type to core-shell with higher Cu:Ag precursor ratio. When applied in CO_2RR catalysis, the nanoparticles configuration appears to matter more than the exact Cu:Ag composition. The core-shell arrangement is found to have higher C_{2+} production over Janus-type, posited due to its ability to retain more Cu-Ag interface during CO_2RR. Thorough pre- and post- catalysis electron microscopy investigations revealed that Cu-Ag pairing likely resulted in selective oxidation of Cu, resulting in strained Cu_2O-Ag epitaxial relationship that can be retained in the reduced Cu-Ag during CO_2RR. On the use of electrochemical methods as convenient "probes" to rationalise CO_2RR activity, we found ECSA and EIS measurements to be ineffective in predicting CO_2RR product selectivity. Instead, surface charge estimated using modified pulse voltammetry technique is more suitable, where distinct behaviour between Ag and Cu-containing catalysts can be observed. Due to severe reconstruction during catalysis, having a core-shell configuration is found to be more beneficial to the catalysis performance than initial composition. Beyond Cu-Ag, we believe the findings are relevant to many other multi-component catalysts with immiscible constituents.

1. Introduction

Elevated global carbon dioxide (CO_2) concentrations have reached critically alarming levels, contributing to annual emissions exceeding 32 billion tonnes per year [1], with the atmospheric CO_2 burden recognised as the primary driver of contemporary climate change [2]. Among the principal net-zero CO_2 strategies, carbon capture and utilisation (CCU) is arguably the more compelling strategy that allows valorisation of

View Article Online
DOI: 10.1039/D6TA02615J

the captured CO_2 into renewable feedstocks for the chemical industry [3]. A key strategy for effective CCU lies in the design of advanced electrocatalysts that can efficiently and selectively convert CO_2 into valuable carbonaceous products [4]. Electrochemical CO_2 reduction allows the integration of CO_2 splitting and hydrogenation within a streamlined continuous process [5]. Furthermore, its compatibility with on-demand renewable energy sources that are becoming cost-effective (as low as US$ 0.03/kWh for solar [6] and US$ 0.02/kWh for wind [7]), offers the potential for profitable, zero- or negative-emission industrial chemical production when deployed at scale [8, 9].

Copper (Cu) is the most prominent single metal catalyst capable of reducing CO_2 into a myriad of multi carbon products [10, 11]. To enhance its CO_2RR activity, researchers have proposed to combine Cu with different metals to form Cu-containing bi- or multimetallics (including alloys or composites) that may display synergistic effects. Amongst the different bimetallics, Cu-Ag stood out, with no less than 100 published literatures demonstrating a significant boost in CO_2RR activity in the past decade. By itself, Ag is one of the most active catalysts for CO_2RR to CO [12], and heightened production of CO is commonly present in the majority of Cu-Ag bimetallics [13]. However, there are other bodies of work that do not show increased CO production, especially those with smaller fractions (<10 at%) of well mixed Ag [14].

One of the most popular explanation to the enhanced CO_2RR on Cu-Ag alloys or mixtures is the “CO spillover effect”, ascribed to the utilisation of produced CO (g) or transfer of adsorbed *CO intermediates from Ag sites to the neighbouring Cu sites that allows higher *CO coverage and enhanced C-C coupling activity [15, 16]. Alternatively, Clark et al. proposed that compressive strain imposed on Cu atoms, especially on the surface of bulk Cu-Ag bimetallics, is the pertinent reasoning behind the enhanced C_{2+} selectivity [17]. More recent study using In-situ nanofocused X-ray absorption spectroscopy revealed the dynamic nature of the atomic arrangement and strain within Cu-Ag Janus-type particles [18].

Several major complications of Cu-Ag for CO_2RR are their immiscibility, very high mobility of both Cu and Ag atoms, and the galvanic corrosion. Recalling that Cu-Ag is a eutectic system with two terminal solid solutions [19], Cu-Ag bimetallic is not likely to exist in an alloyed form at room temperature, but rather as segregated solid phases, even near either end of the phase diagram [20, 21]. To gain some control over the segregation behaviour in Cu-Ag bimetallics many have proposed engineered microstructures, such as core-shells [22], Janus [23] or extremely small (<2 nm) nanoparticles [24], which typically mandates the addition of polymeric surfactant or other ligands. Synthesising Cu-Ag bimetallics with good composition and size control without any surfactant or ligand is significantly more challenging. Even with some initial control during synthesis, we expect that surface reconstruction of Cu-Ag bimetallics under CO_2RR will be more severe compared to bare Cu due to the combined dynamic effects of the galvanic corrosion [25, 26] and surface reactions facilitated by water/hydroxyls [27]. This reconstruction process often result in irregular and much smaller particles compared to the initial form, especially those containing lower (<20%) Ag content [16]. Conversely, Cu-Ag bimetallics with higher (>20%) Ag content tend to show a larger chunk of Ag-rich sections that are more resistant to reconstruction [28-30].

Besides complex high vacuum deposition and ablation techniques that requires expensive high purity metal targets [16, 31], atmospheric pressure plasma jet (APPJ) is a powerful and versatile alternative technique. APPJ is capable of depositing ligand-free multi-component nanosized metals from aqueous metal salt without the need for any vacuum or extreme heating [32-35]. Here, we found that APPJ can

View Article Online
DOI: 10.1039/D6TA02615J

consistently synthesise CuO_x-Ag composite films consisting of conjoined (Janus) or core-shelled particles with Cu:Ag ratio matching the initial precursor ratio. Galvanic pairing effect inevitably converts Cu to CuO_x, which serendipitously facilitates the epitaxial relationship between Cu and Ag. Films with higher Ag fractions (≥60%) were found to produce C_{2+} liquid products favourably. Extensive high resolution electron microscopy and elemental analyses, alongside electrochemical characterisation, provided a clue that the majority of Ag tends to aggregate together either as the inner core in core-shell arrangement or distinct section in Janus type particles. We found that core-shell arrangements are more favourable over Janus-type arrangements as the former retains more Cu-Ag interface during CO_2RR.

2. Results and Discussion

2.1. Cu-Ag composites with varying metal ratios as efficient electrocatalysts for CO_2 reduction.

The CO_2RR product distribution from electrodes synthesised on APPJ grown CuO_x-Ag composites with rising Cu content were investigated. Cu_0Ag_{100} (pure Ag) was taken as a baseline, showing the expected CO as the main CO_2RR product (**Fig 1a**). The addition of small amounts (5 at%) of Cu (Cu_5Ag_{95}) still yielded in CO as the main CO_2RR product, but this time with extended H_2 evolution suppression towards more cathodic potentials up to -1.6 V (**Fig 1b**). A striking observation is the appearance of liquid C_2 oxygenate (ethanol, FE_{C2H5OH} >3.7%) at -1 V that was accompanied with only trace amounts of the corresponding alkene (ethylene, FE_{C2H4} <0.27%), representing an ethanol/ethylene ratio of >14 (**Fig 1g**). Dominant ethanol production over ethylene was still observed with more cathodic potential on Cu_5Ag_{95}, albeit with reduced ethanol/ethylene ratio of ≈2 at -1.6 V. With increasing Cu content, the production of ethanol and n-propanol increases significantly; at -1.2 V, FE_{C2H5OH} >12.7% and FE_{C3H7OH} >3.0% were recorded for $Cu_{20}Ag_{80}$ (**Fig 1c**), while FE_{C2H5OH} >13.6% and FE_{C3H7OH} ≈3.9% for $Cu_{40}Ag_{60}$ (**Fig 1d**). The total FE for 2- and 3-carbon liquids totalled to ≈20% for $Cu_{20}Ag_{80}$ and $Cu_{40}Ag_{60}$. Increasing Cu fraction of the CuO_x-Ag composites was found to be counterproductive, with diminishing FE_{C2+} selectivity observed when the Cu fraction is >60% (**Fig 1e-f**), with the overall product distribution start to resemble pure bulk Cu (**Fig S1b**).

Generally, our APPJ-grown films displayed higher ethanol/ethylene ratio compared to pure Cu (**Fig 1g**), with lower Cu fractions (5-40%) films displaying more than twice the typical 0.4 – 0.5 ratio reported on bulk Cu or oxide-derived Cu catalysts [11, 36]. In the literature, CO_2RR pathway towards ethanol on bare Cu has been shown to branch out from C_2H_4 at *CH-COH [37, 38], where ethanol formation is more endothermic by 0.43 eV. Strategies to steer CO_2RR production to higher ethanol/ethylene ratio has been reported by using higher KOH electrolyte concentration [39], or by modifying the Cu surface with N-containing [40, 41] or S-containing [42] organic ligands. Further, the majority of CO_2RR on Cu-Ag bimetallics typically display FE_{C2H5OH}/FE_{C2H4} ratio less than 1 [13-18, 43], with the exception of reports from Wang et al. (ratio: 1.17) [44] and Gao et al. (ratio: 8) [45]. A more comprehensive comparison with other Cu-Ag literature is presented in **Table S7**. As no organic ligands were added in our APPJ-grown films, we posit that the favourable ethanol production should be attributed to weaker *O binding energy and the more difficult O-C bond cleavage for $*OCHCH_2$ on strained Cu-Ag compared to pure Cu [18, 46].

Partial current densities for C_{2+} products (j_{C2+}) are plotted in **Fig 1h** (C_1 products and H_2 in **Fig S2a-b**) to estimate CO_2RR turnover. The optimum potential to produce C_{2+} products was at -1.4 V vs RHE for most catalyst except $Cu_{40}Ag_{60}$ that has slightly higher turnover at -1.2 V. APPJ grown CuO_x-Ag composites generally outperforms pure Cu up to $Cu_{60}Ag_{40}$, but higher Cu:Ag ratio starts to follow the trend of pure Cu.

View Article Online
DOI: 10.1039/D6TA02615J

Overall, $Cu_{40}Ag_{60}$ appears to display the highest C_{2+} selectivity, followed by $Cu_{20}Ag_{80}$. Further characterisation will focus on these catalysts.

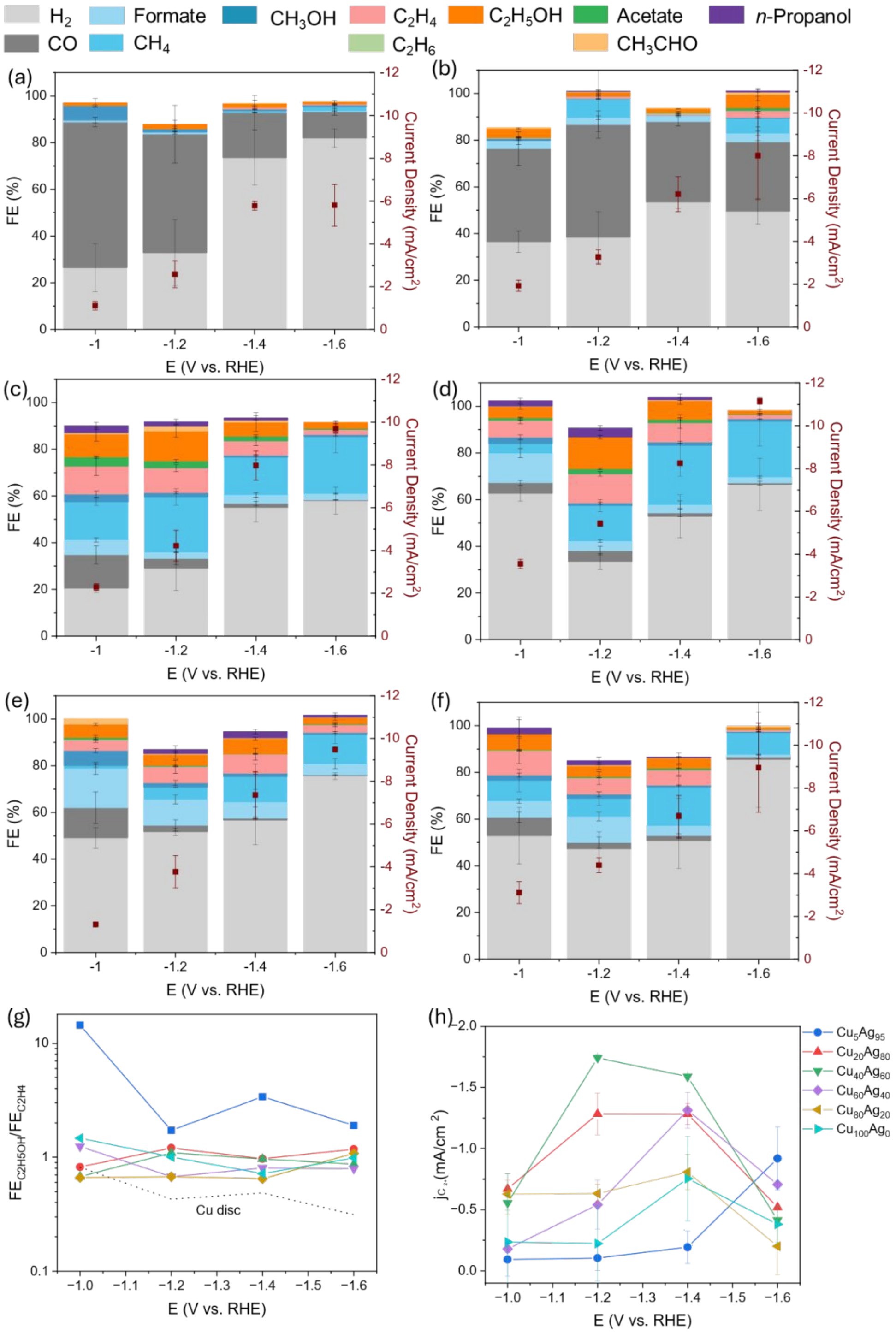

Figure 1: Average of steady state CO_2RR Faradaic efficiencies (FE) for gaseous and liquid products against the various applied potentials (V vs. RHE) during 1.5 hrs of electrolysis on (a) Cu_0Ag_{100}, (b) Cu_5Ag_{95}, (c) $Cu_{20}Ag_{80}$, (d) $Cu_{40}Ag_{60}$, (e) $Cu_{60}Ag_{80}$, and (f) $Cu_{80}Ag_{20}$. (g) FE_{C2H5OH}/FE_{C2H4} ratio and (h) partial current density for multi carbon products (j_{C2+}) on Cu_5Ag_{95} to $Cu_{100}Ag_0$. Each point represents an average of three independent measurements, and the error bar represents the standard deviation.

View Article Online
DOI: 10.1039/D6TA02615J

2.2. Characterisation of as synthesised $Cu_{20}Ag_{80}$ and $Cu_{40}Ag_{60}$

We focused our investigations on $Cu_{20}Ag_{80}$ and $Cu_{40}Ag_{60}$ that display the best steady state CO_2RR Faradaic efficiencies (FE). SEM characterisation revealed that the higher Ag content $Cu_{20}Ag_{80}$ film consists of larger (*ca.* 100-200 nm) primary particles (**Fig 2a-b**), whereas $Cu_{40}Ag_{60}$ consists of larger aggregates (**Fig 3a-b**). High-angle annular dark-field (HAADF) imaging, scanning transmission electron microscope energy dispersive spectroscopy (STEM-EDS) mapping, and high-resolution TEM micrographs, however, tell a more interesting story. We discovered that the primary particles of the lower Cu content $Cu_{20}Ag_{80}$ is of Janus-type particles, with distinct segregation between Cu-rich and Ag-rich regions (**Fig 2d-g**). On the other hand, $Cu_{40}Ag_{60}$ has a core-shell type primary particles, consisting of Ag-rich core and Cu-rich shell (**Fig 3d-g**). As there is no surface directing agent or linker used and identical APPJ procedure was adopted, we expect the factor determining the particle type is the molar ratio between $Cu(NO_3)_2$ and $AgNO_3$ precursors.

The plasma used in APPJ is considered non-equilibrium plasma, consisting of energetic electrons and "cold" neutral and ionic species [34, 47, 48]. Therefore, the majority of solvent droplets carrying Cu-Ag precursors should not evaporate immediately, allowing energetic surface electron irradiation to drive diffusion, transport and reaction (e.g., metal reduction) [49]. Transitions between core-shell to Janus has been observed for uncapped Cu-Ag bimetallic nanoparticles, driven only by temperature and increasing Ag composition [50]. In our case, although the bimetallics formation is driven by energetic electrons within the plasma, we posit that similar effects can still occur *within* the tiny vapour droplets carrying well mixed Cu-Ag precursors without any surface directing agents, resulting in clear transition between Janus and core-shell when Cu:Ag fraction is tuned. Although N_2 sheath gas was applied during APPJ synthesis, EDS distribution map for our samples still detected significant amounts of oxygen, especially around the Cu-rich regions on both $Cu_{20}Ag_{80}$ and $Cu_{40}Ag_{60}$ that points to possible CuO_x formation (**Fig 2g, Fig 3g**, and line EDS in **Fig S4**). Although the deposition of single component Cu and Ag in metallic form have been demonstrated previously [34], we believe the selective oxidation of Cu in the Cu-Ag bimetallic configuration may be inevitable due to the galvanic corrosion effect [51].

Closer scrutiny of the particle and the interface between Cu-rich and Ag-rich regions using HRTEM confirmed that the crystal structure of the Cu-rich region is consistent to Cu_2O lattice. On the Cu-rich section of $Cu_{20}Ag_{80}$ sample (**Fig 2h**), the *d*-spacing perpendicular to the Cu_2O-Ag interface (i.e., Cu_2O $d_{(1\text{-}11)}$) was found to be ≈0.240 nm, which is close to the relaxed Cu_2O $d_{(111)}$ of 0.2464 nm [52]. The Ag $d_{(111)}$ near the Cu-Ag boundary was found to be 0.230 nm, which is also close to the expected value for bare Ag (≈0.236 nm) [53]. However, electron diffraction analysis (calculated using fast Fourier transform (FFT) from the HRTEM micrographs, inset of **Fig 2h**) revealed closely matched Ag and Cu_2O lattice in the [011] direction, which indicates significant strain to the Cu_2O lattice. This supposition is also supported by the strain analysis based on the d-spacing variation (**Fig S7**).

View Article Online
DOI: 10.1039/D6TA02615J

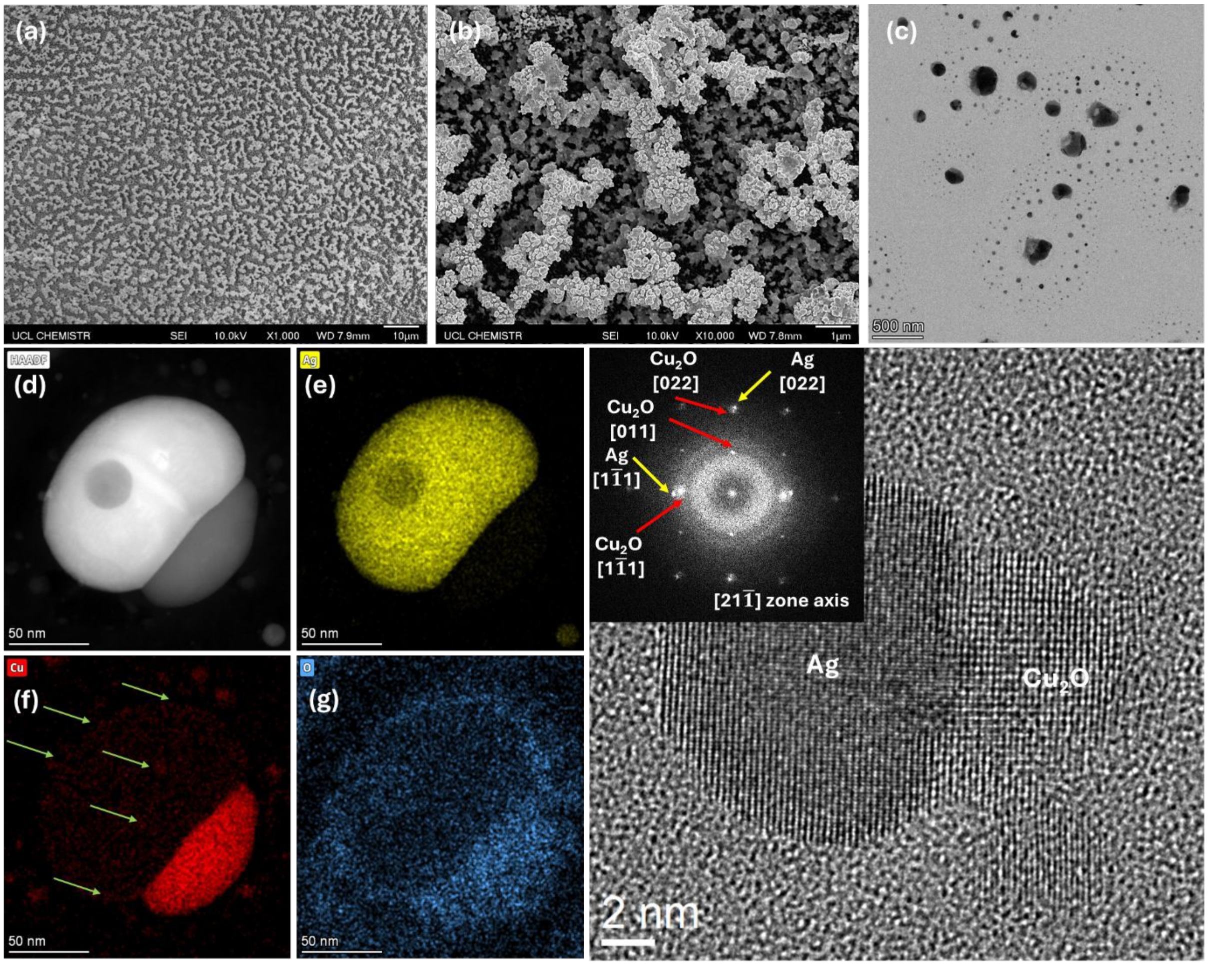

Figure 2: Electron microscopy characterisation of APPJ synthesised $Cu_{20}Ag_{80}$ bimetallic. (a) Low and (b) high magnification FE-SEM of $Cu_{20}Ag_{80}$ deposited on glassy carbon substrate. (c) Low magnification TEM, (d) high angle annular dark field TEM and electron dispersive spectroscopy mapping of (e) Ag, (f) Cu, and (g) O elements. Green arrows on sub-figure (f) indicate traces of Cu that are deposited around the Ag-rich part. (h) High resolution TEM of representative APPJ grown $Cu_{20}Ag_{80}$ alongside $[21\bar{1}]$ zone axis, showing sharp Cu_2O-Ag boundary. The inset of subfigure (h) shows simulated electron difraction of the particle generated by fast Fourier transform calculation, showing closely aligned Cu_2O and Ag lattices, with compressed Cu2O lattice along [011] direction but relaxed along [111]. (c-h) is taken on samples directly grown on SiN_x TEM grid.

On $Cu_{40}Ag_{60}$, the observed Cu_2O $d_{(111)}$ of 0.242 and Ag $d_{(111)}$ of 0.230 nm (**Fig 3h**) are also close to the respective bulk values. Like the $Cu_{20}Ag_{80}$ samples, very close crystallographic relationship between Cu_2O and Ag was also observed on $Cu_{40}Ag_{60}$. Due to the core-shell nature of the particle that causes overlapping crystal orientations, the electron diffraction pattern can only reveal closely aligned Cu_2O(111) and Ag(111) planes perpendicular to the Ag-Cu_2O interface (inset in **Fig 3h**), indicative of an epitaxial-like relationship. However, we believe similar strain observed alongside the Ag-Cu_2O interface should operate in the core-shelled particle.

In the literature, epitaxial relationship between metallic Cu-Ag is difficult to achieve due to the large lattice mismatch (12.6%) [52, 53]. To our knowledge, true epitaxial growth of metallic Cu-Ag can only be achieved via surface limited redox replacement reaction of monolayer sacrificial metal (typically Pb)[54] or by introducing large amounts of twin boundaries on either Cu or Ag seed crystals in presence of galvanic corrosion suppression agents [51]. Serendipitously, oxidation of Cu-rich region in our samples makes stable epitaxial relationship between oxidised Cu_2O and Ag more facile. On the (111) plane especially, the lattice mismatch between Ag and Cu_2O (4.3%) is significantly smaller than between Cu-Ag (>12%). It is notable that our APPJ synthetic approach can readily achieve Cu_2O-Ag epitaxial-like relationship without adding any surface capping agents or other additives. As the lattice of both Ag and Cu_2O are almost fully relaxed, we believe that the epitaxial-like relationship in APPJ grown Cu_2O-Ag composites observed here can be maintained until it is ready for use as CO_2RR catalyst.

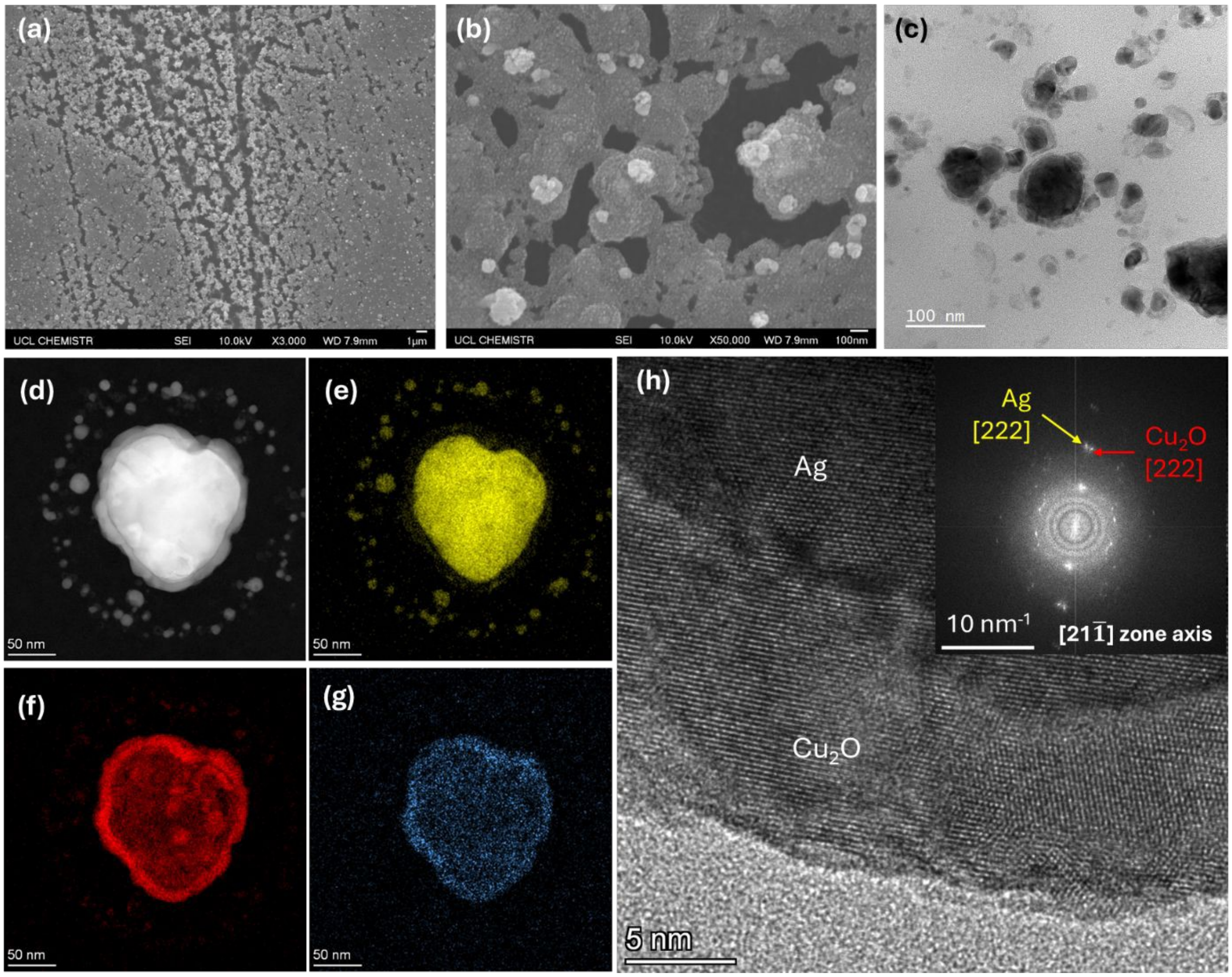

Figure 3: Electron microscopy characterisation of APPJ synthesised $Cu_{40}Ag_{60}$ composite. (a) Low and (b) high magnification of field emission electron scanning microscopy of $Cu_{40}Ag_{60}$ deposited on glassy carbon substrate. (c) Low magnification transmission electron microscopy (TEM), (d) high angle annular dark field TEM and electron dispersive spectroscopy mapping of (e) Ag, (f) Cu), and (g) O elements. (h) High resolution TEM of representative $Cu_{40}Ag_{60}$ showing less defined boundaries between Ag and Cu_2O regions and existence of multiple crystal orientations. Inset in (h) shows FFT generated electron diffraction, showing closely aligned Cu_2O [222] and Ag [222]. (c-h) is taken on samples directly grown on SiN_x TEM grid.

Overall, the elemental analyses from TEM and SEM EDS demonstrates good control of Cu-Ag composition in the APPJ synthesised composites, where the actual Cu:Ag ratios are within 2% of the intended precursor values (**Table 1, Table S2**). Curiously, the surface composition probed by XPS indicated very high surface Cu:Ag ratio for both samples. Whilst high surface Cu is expected for $Cu_{40}Ag_{60}$ that has a core-shell structure, the observation of high surface Cu on $Cu_{20}Ag_{80}$ suggests that Cu deposition maybe spread more

View Article Online
DOI: 10.1039/D6TA02615J

widely than expected. Closer inspection of the TEM EDS mapping on $Cu_{20}Ag_{80}$ shows traces of smaller Cu particles that likely surround the Ag-rich regions (green arrows on **Fig 2f**).

2.3. Characterisation of $Cu_{20}Ag_{80}$ and $Cu_{40}Ag_{60}$ post CO_2RR

Changes on CuO_x-Ag composites after CO_2RR can be discombobulating due to compounding effects of cathodic potential, galvanic effect, surface reactions, and post-catalysis reoxidation that require comprehensive analysis using multiple analytical tools [25, 26].

Starting with HAADF and STEM-EDS analyses, the most significant reconstruction is found on $Cu_{20}Ag_{80}$, where the Janus arrangements disappear after CO_2RR. Instead, smaller particles with significantly more dispersed Cu are observed and lower oxygen signal than the as-prepared samples (**Fig 4a-d, Fig S5a-c**). A closer inspection of $Cu_{20}Ag_{80}$ lattice using HRTEM reveals practically unchanged Ag-rich region (Ag $d_{(111)}$ ≈0.230 nm) but more spread-out Cu-rich region with difficult to discern lattice spacing (**Fig 4e**). Statistical TEM particle analysis (**Fig S6a, Table S1**) detected a slight reduction of mean particle size of $Cu_{20}Ag_{80}$ from 28.4 nm to 24.3 nm after CO_2RR, suggesting possible partial dissolution during catalysis.

While copper oxides are generally expected to be reduced during CO_2RR, re-oxidation within 60 seconds of voltage removal to a mixture of Cu_2O and other lesser defined Cu species has been observed [55]. To explain the findings, post-CO_2RR XPS is performed on the spent electrodes. Comparison of high-resolution Cu *2p* spectra (**Fig S16a, S16c**) clearly shows suppression of the Cu satellite peaks after catalysis, suggesting at least partial surface reduction to a possible mixture of $Cu^{(0)}$ and $Cu^{(I)}$ mixture post CO_2RR. Cu LMM Auger spectra shows the presence of mixed oxidation state after CO_2RR (**Fig S16e**), with dominant $Cu^{(I)}$ [56]. On the other hand, comparison of Ag 3d spectra (**Fig S16b, S16d**) detected complete disappearance of Ag (I) peaks after CO_2RR, suggesting significant re-oxidation resistance of Ag. Taken together, these observations indicate more severe changes on Cu compared to Ag in the $Cu_{20}Ag_{80}$ Janus structure, possibly leading to Cu redistribution throughout the electrode.

The reconstruction on the $Cu_{40}Ag_{60}$ sample looks rather different. Large sections (>100 nm) of Ag-rich particles are readily found post CO_2RR (**Fig 4f-g, Fig S5d-e**). Most importantly, significant amounts of Cu are still observed to congregate around the Ag-rich core (**Fig 4h, S4f**), suggesting that the core-shell morphology is relatively preserved. In contrast with $Cu_{20}Ag_{80}$, statistical TEM particle analysis of $Cu_{40}Ag_{60}$ (**Fig S6b, Table S1**) indicates growing mean particle size from 46.2 to 60.1 nm after CO_2RR, suggesting possible agglomeration after catalysis. Although we could not discern the lattice spacings for $Cu_{40}Ag_{60}$ HRTEM post CO_2RR, the core-shell construction in the individual particles can still be observed, with the lighter contrast on the shell likely to be re-oxidised copper (**Fig 4j**). Post CO_2RR XPS analysis of Cu *2p* and Ag *3d* shows similar behaviour like $Cu_{20}Ag_{80}$, where the Cu satellite peaks are significantly reduced post catalysis (**Fig S14a, S14c**), and the Ag(I) shoulder is completely removed (**Fig S14b, S14d**). A similar shift in Cu LMM peak kinetic energy is also observed (**Fig S14e**), suggesting formation of mixed Cu species after CO_2RR with dominant $Cu^{(I)}$.

The distinct modes of reconstruction on both samples are also corroborated using elemental analyses. The bulk Cu fraction of $Cu_{20}Ag_{80}$ (measured by TEM EDS), dropped from 18.9% to 8.3% post CO_2RR, while much smaller reduction from 41.4% to 35.2% was observed on $Cu_{40}Ag_{60}$ (**Table 1**). On the contrary, a

View Article Online
DOI: 10.1039/D6TA02615J

pronounced increase in surface Cu fraction (measured by XPS), from ≈84% to >91% was detected on $Cu_{40}Ag_{60}$, compared to 82% to 87% on $Cu_{20}Ag_{80}$.

While significant mobility of both Cu and Ag are expected during catalysis[57], the different reconstruction modes observed on $Cu_{20}Ag_{80}$ and $Cu_{40}Ag_{60}$ suggests that the initial core-shell structure encourages better retention of Cu-Ag interface during CO_2RR than in Janus-type particles. To support this position, ICP OES analysis of the spent catholytes were performed (**Table S5, Fig S18a**). Expectedly, higher leached Cu absolute concentration was detected due to higher absolute initial loading on samples with higher Cu fraction. However, when normalised to the Cu fraction, non-uniform U-like response was observed, suggesting lower normalised Cu leaching rate on $Cu_{40}Ag_{60}$ compared to $Cu_{20}Ag_{80}$. We also note generally more stable C_2H_4 turnover on the core shell $Cu_{40}Ag_{60}$ (≈3% reduction from t = 20 mins to t = 80 mins, **Fig S3b**) compared to $Cu_{20}Ag_{80}$ (≈30% reduction, **Fig S3a**)

Table 1: Elemental analyses of $Cu_{20}Ag_{80}$ and $Cu_{40}Ag_{60}$ tracking Cu and Ag before and after CO_2 reduction reaction using TEM EDS (representing bulk composition) and XPS (representing surface composition).

	TEM EDS (at%)			XPS (at%)		
	Cu	Ag	Std Dev	Cu	Ag	Std Dev
$Cu_{20}Ag_{80}$ as grown	18.89	81.12	2.27	82.12	17.88	1.00
$Cu_{20}Ag_{80}$ post CO_2RR	8.26	91.75	2.40	86.99	13.01	0.78
$Cu_{40}Ag_{60}$ as grown	41.40	58.60	3.37	84.31	15.69	1.24
$Cu_{40}Ag_{60}$ post CO_2RR	35.19	64.81	8.09	91.26	8.74	1.51

View Article Online
DOI: 10.1039/D6TA02615J

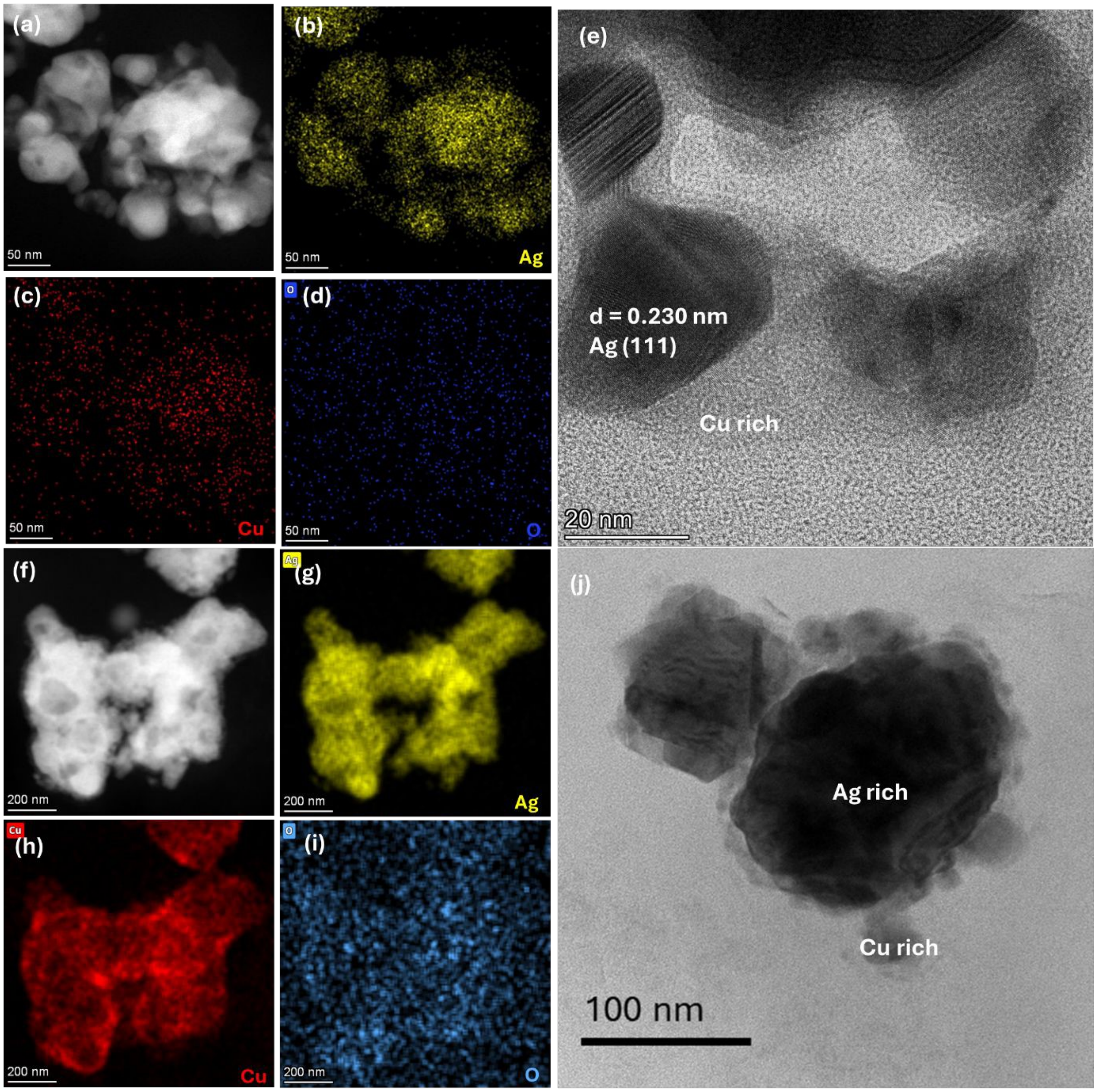

Fig 4: Post CO_2RR characterisation using HAADF, TEM-EDS mapping, and HRTEM for (a-e) $Cu_{20}Ag_{80}$ and (f-i) $Cu_{40}Ag_{60}$, performed on scraped Cu-Ag samples on glassy carbon substrates, resuspended in isopropanol, and deposited on holey carbon TEM grid.

2.4. Electrochemical Characterisations

Electrochemical characterisations were also carried out to supplement physical characterisation data. First, electrochemically active surface area (ECSA) was estimated using multiple CV runs at 14 different scan rates and double layer capacitance (C_{DL}) extracted from current density and scan rate relationship (**Fig S4a-b**). Overall, incorporation of Cu into Ag appears to increase the overall C_{DL} from 0.5 mF displayed by Cu_0Ag_{100} to about 0.8 mF for $Cu_{60}Ag_{40}$ (**Fig S4c**). However, as there are mixed elements in the composite, it is difficult to ascertain if the small increments in the C_{DL} values are directly linked to larger surface area.

View Article Online
DOI: 10.1039/D6TA02615J

We then turned to EIS to probe the samples further. Near the open circuit potential (OCP), films with larger Cu:Ag fraction samples showed lower charge transfer resistance (R_1) reflected roughly by the diameter of the semicircles (**Fig S9a**). However, EIS measurements at OCP could not be relevant to the catalytic process, as the catalyst surface and Helmholtz plane composition will be substantially altered upon external voltage application beyond catalytic onset [58]. A more representative and quantitative metrics can be extracted from EIS data at or near CO_2RR relevant potentials using numerical fitting procedure [40, 58]. Numerical fitting results using the Armstrong-Henderson equivalent circuit that considers electrochemically adsorbed intermediates (**Fig S9c**) [59, 60] is displayed in **Fig S10**. The resistive components of R_1 and R_2 decreased exponentially with more cathodic applied voltage, while the capacitive elements (CPE_1 and CPE_2) showed different responses. CPE_1 generally display a relatively flat response towards the applied voltage (**Fig S10b**), while exponential changes in CPE_2 were observed (**Fig S10d**). Whist R_1 may be the preferred metric to explain simpler electrocatalytic reaction like water splitting [58], we posit that the longer timescale CPE_2 is more relevant to multi-stepped electrocatalytic process like CO_2RR to C_{2+} that require intermediate accumulation and non-electrochemical C-C coupling step [61]. Unfortunately, attempts to find a correlation between electrochemically measured metrics, through either ECSA and EIS, and FEC_{2+} did not reveal any strong correlation (Pearson's $|r| \approx 0.02$ to 0.28, **Fig S11**). Weak correlation between R_1 and FEC_{2+} also suggests that CO_2RR to C_{2+} on Cu-Ag in our experiment may not operate in charge transfer limited region.

Additional analyses were carried out modified pulse voltammetry (mPV) measurement, involving stepwise change from open circuit potential (OCP) to progressively more cathodic voltage (**Fig S12**). mPV has been shown to correlate well to CO_2RR activity of organic-functionalised Cu [40]. Here, we believe it may also be applicable to metal combinations and bimetallics. Specifically, the integrated anodic charge (Q_{an}) measured during potential reversal from applied cathodic potentials to near OCP is proposed to be proportional to the electrochemically absorbed species on the catalyst surface (see **SI Section 6** for further information). Tabulation of Q_{an} values with respect to ΔV presented **Fig 5a** show distinct characteristics of catalysts with and without Cu addition. Samples without Cu (i.e., Cu_0Ag_{100}) display relatively flat Q_{an} values with increasing ΔV, indicative of low accumulation of adsorbed species and consistent with Ag's inherently weak interaction with *CO (a crucial intermediate for CO_2RR to C_{2+}) [62]. When Cu is added in the bimetallic, we observed a significant "jump" in Q_{an} when $\Delta V > 0.8$ V. This voltage range coincides with *CO accumulation event that preceded C_{2+} formation during CO_2RR on Cu reported previously [11, 61]. Additionally, a strong correlation between Q_{an} and j_{C2+} at -1.4 V vs. RHE on Cu-Ag bimetallics at comparable applied voltage is observed (Pearson's $r = -0.85$, **Fig 5b**).

View Article Online
DOI: 10.1039/D6TA02615J

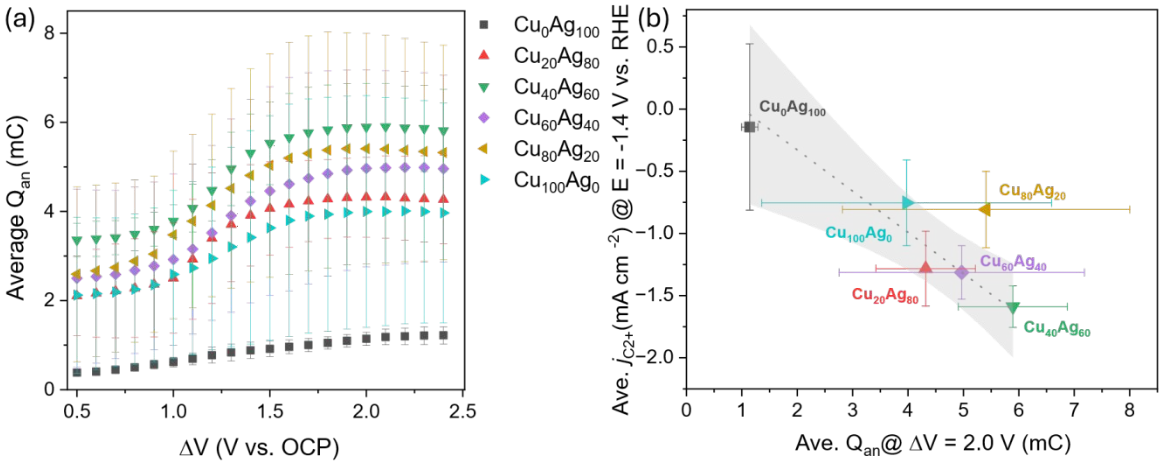

Fig 5: (a) Integrated anodic charge (Q_{an}) of APPJ-deposited CuAg bimetallics with increasing ΔV. The X axis "ΔV" represents voltage difference between the applied pulse and the OCP, which varies slightly on each material. Roughly, ΔV = 1.6, 1.8, 2.0 and 2.2 correspond to catalytic potentials of -1.0, -1.2, -1.4 and -1.6 V vs. RHE. Data were obtained as the average of 3 independent replicates. (b) Correlation plot between average j_{C2+} at -1.4 V vs. RHE and Q_{an} at ΔV = 2.0 V for APPJ deposited CuAg bimetallics. Dotted line represents York linear fitting (Pearson's *r* = -0.85) that considers both X and Y errors, while grey shading marks the 95% confidence interval bands.

Discussion

There are two popular explanations in the literature for the enhanced CO_2RR to C_{2+} on Cu-Ag bimetallics. Early works appear to favour the "CO spillover" explanation, where the enhanced C_{2+} products on Cu-Ag are always accompanied by a concomitant increase in CO(g) production [15, 16]. The premise of this hypothesis is that some of the adsorbed *CO or the CO(g) produced in Ag sites can be transferred to the neighbouring Cu sites, enabling better *CO accumulation. Other researchers had different ideas, as the CO(g) production appears to be proportional to surface Ag content post CO_2RR, and the enhanced C_{2+} production should instead be linked to the compressive strain to the Cu lattice [17]. Albeit with a smaller dataset, a relatively more linear j_{CO} relationship with varying Cu:Ag fraction is also found in this work, but much less so for j_{C2+} (**Fig S13**). As such, we are inclined to concur that the enhanced C_{2+} production should be ascribed to a much more fundamental change in the active catalyst structure rather than a simple *CO spillover effect.

Extensive TEM experiments in this work unveiled that the Cu rich region in our APPJ grown Cu-Ag is readily oxidised to Cu_2O structure, even though individual metallic Cu and Ag growth using the same technique has been demonstrated previously [34]. We believe this is due to the Galvanic effect and should be universal to pairings between Cu and more noble metals without any surface capping agent or linkers. Fortuitously, oxidised Cu_2O still has a matching ($Fm\bar{3}m$) space group with Ag, with significantly smaller lattice mismatch than metallic Cu-Ag pair, allowing stable Cu_2O-Ag epitaxial-like relationship. Additionally, Cu_2O should also experience roughening phenomenon during the initial reduction phase and bring about the oxide-derived Cu benefit [55].

After CO_2RR, significant reconstruction of the catalysts was observed that more severely affecting $Cu_{20}Ag_{80}$ catalyst. On this sample, Janus arrangements can no longer be found, accompanied by significant Cu redistribution away from Ag. On the other hand, the core-shell configuration on $Cu_{40}Ag_{60}$ can still be

View Article Online
DOI: 10.1039/D6TA02615J

readily found, with a significant majority of Cu is still surrounding the Ag-rich core. HRTEM investigation revealed post catalytic conversion of Cu species to less well defined oxidised structure. XPS analyses shows that both samples are generally more reduced after CO_2RR to $Cu^{(I)}$ dominated mixture, accompanied by suppression of the satellite peaks consistent with $Cu^{(II)}$.

Between $Cu_{20}Ag_{80}$ and $Cu_{40}Ag_{60}$, we believe that the morphology of the initial Cu-Ag bimetallics may be more dominant in determining CO_2RR activity than the absolute Cu:Ag ratio. As our CuO_x-Ag composites are not functionalised by any ligand, the morphology change is entirely driven by Cu:Ag ratio and thermodynamics [50]. While we expect that the in-situ epitaxial relationship between Cu_2O and Ag to be morphology agnostic, the core-shell microstructure may have a competitive edge due to its ability to retain more Cu in direct contact with Ag core during CO_2RR. The closer proximity of CuO_x shell to Ag core can also reduce Cu redistribution significantly during the initial phase of reduction. With a matching $Fm\overline{3}m$ space group, Ag is still a preferred Cu (re)nucleation site compared to random surfaces like glassy carbon due to lower activation free energy for nucleation[63]. This advantage is also reflected in a more stable C_2H_4 turnover on $Cu_{40}Ag_{60}$ (only about 3% degradation after 80 mins) compared to $Cu_{20}Ag_{80}$ that shows >30% decrease over the same period (**Fig S3**). As the Cu_2O is expected to reduce to metallic Cu during CO_2RR, we believe the reduced Cu will be forced to keep its *tensilely* strained state conforming to the Ag lattice under applied cathodic bias. Such voltage-dependent strain behaviour has been reported on Cu-Ag particles using nano-focused X-ray [18], where the larger tensile strain on Cu side of the Janus can be retained under cathodic bias. Additionally, tensile strain in Cu lattice has been shown using DFT to increase *CO binding strength and, more importantly, reduces $\Delta G_{formation}$ for C_{2+} intermediates on Cu [64].

We also acknowledge the possibility that true Cu-Ag alloying contributes to the enhanced CO_2RR activity. Although we cannot conclusively demonstrate existence of Cu-Ag alloying in very small particles (<10 nm) after CO_2RR, there are at least two papers, [24, 65] where α-phase (Ag rich) can exist up to 28% Cu:Ag ratio in very small (5 nm) nanoparticles. However, due to severe reconstruction of the catalysts under reaction conditions, we posit that the precise initial composition of alloys, especially in immiscible metal pairings like Cu-Ag, may not matter too much as the metal pairs tend to segregate during reaction. Instead, having an initial core-shell configuration, with a thin layer of the active species shell facing the reactant, is more critical as the active species will remain anchored to the stable core, whilst allowing strain effect to kick in.

On the use of electrochemical methods as convenient "probes" to rationalise CO_2RR activity, we found ECSA, and charge transfer resistance parameters extracted from numerical fittings of EIS measurements to be ineffective in predicting C_{2+} activity amongst CuO_x-Ag composites (**Fig S11**). This is consistent with literatures as CO_2RR to C_{2+} involves non-electrochemical coupling step that is limited to the surface *CO coverage [61, 66] instead of charge transfer kinetics. We found that a more suitable metric is the surface charge estimated using mPV, where distinct behaviour between Ag and Cu-containing catalysts are observed (**Fig 5**). Potentially, we believe that surface charge estimation using mPV can be applied to multi-metal catalysts, in addition to organic functionalised Cu demonstrated earlier [40].

3. Conclusion

View Article Online
DOI: 10.1039/D6TA02615J

This research provides critical information in the quest to understand multi-stepped CO_2RR on bimetallics structure. Based on comprehensive electron microscopy study that tracks the evolution of ligand-free CuO_x-Ag composite from its growth using APPJ to its reconstruction after CO_2RR, we believe the enhanced C_{2+} production on Cu-Ag should be ascribed to a much more fundamental change in the active catalyst structure rather than *CO spillover. One of such change is the tensile strain on Cu lattice that can be brought about by applied cathodic potential that can force reduced Cu to conform to Ag lattice. Epitaxial relationship between Cu_2O and Ag is observed on APPJ grown films, accommodated by the initial oxidation of Cu due to galvanic corrosion upon pairing with the more noble Ag. Although this configuration inevitably evolved during CO_2RR, we believe the applied cathodic potential can provide the necessary driving force to keep the Cu-Ag epitaxial relationship in the re-nucleated Cu. Evidence of smaller Cu nuclei surrounding larger Ag-rich regions that retains some epitaxial Cu-Ag relationship supports previous literature on dynamic structure-strain relationship on Cu-Ag. Further, we believe that the morphology of the initial CuO_x-Ag composite may be more important in enhancing the CO_2RR activity than the absolute Cu:Ag ratio. In our APPJ grown films, a moderate Cu:Ag around 40:60 allows formation of Ag@Cu_2O core-shell arrangement is beneficial as it exposes and better retains the more active species (strained Cu-Ag interface) during CO_2RR. In addition to advancing green electrocatalyst development, this work underscores the potential of APPJ in developing catalyst materials with controllable compositions and morphology for scalable, sustainable carbon capture and utilisation (CCU) technologies.

4. Methodology

4.1. Atmospheric pressure plasma jet (APPJ) deposition of Cu-Ag alloy thin films under various ratios

Synthesis and deposition of Cu-Ag bimetallics using APPJ was performed according to our previous work with 20 W effective power [35]. In brief, 96% He gas mixed with 4% H_2 (NOX Singapore) was used as the plasma working gas, ensuring complete reduction of the samples. In brief, Cu-Ag thin films were prepared by nebulising aqueous precursor solutions containing only deionised (DI, 18.2 MΩ.m) water and varying molar ratios of $Cu(NO_3)_2$ and $AgNO_3$. Sample nomenclature $Cu_{20}Ag_{80}$ denotes Cu:Ag precursor composition of 20% (0.1 mM) Cu^{2+} and 80% (0.4 mM) Ag^+. Unless stated otherwise, the total concentration of metal ions in the aqueous solutions was maintained at 0.5 mM for all samples, such that $[Cu^{2+}] + [Ag^+] = 0.5$ mM. All samples were deposited on glassy carbon disks (⌀15 × 1 mm thickness, Goodfellow Cambridge Ltd).

4.2. Electrochemical Methods

Glassy carbon disks were mechanically polished using 5 µm diamond slurry (Struers AG), followed by fine polishing to a mirror finish with a 0.3 µm alumina slurry (Buehler MicroPolish). The substrates were subsequently sonicated in concentrated KOH solution for 10 minutes to remove possible embedded alumina. Post-deposition, the samples were rinsed with deionised water, dried under a N_2 stream, and stored overnight in a dry chamber for 16–18 hours prior to electrochemical experiments. 99.999% purity Cu disks (⌀15 mm × 1 mm thickness, Goodfellow Cambridge Ltd.) were polished with 3 µm polycrystalline diamond slurry followed by sonication in DI water for 1 min. The Cu disks were dried using inert N_2 gas.

4.3. Electrolyte preparation

View Article Online
DOI: 10.1039/D6TA02615J

EMSURE ACS grade $KHCO_3$ (99.7 to 100.5% assay, Supelco) was used for the electrolyte. To minimise dissolved metals in the electrolyte, pre-electrolysis electrolyte cleaning was performed by applying -1 mA for at least 30 mins in a 2-electrode set-up with 2 graphite rods (TedPella, Spec-pure, ⌀1/8" × 20 cm) whilst being purged with CO_2. The $KHCO_3$ 0.1 M electrolyte was initially bubbled and saturated at 20 sccm for 20 mins with CO_2 gas (Linde Gas, 99.999%) using 2 mass flow controllers (MFC, Alicat Scientific MC series).

4.4. Electrochemical CO_2 Reduction Reaction (CO_2RR)

All electrocatalytic experiments were performed in a custom H-Cell made of PEEK and PTFE reported previously [40]. Both anodic and cathodic compartments were filled with 8 ml of CO_2 saturated 0.1M $KHCO_3$. These compartments were separated via an anion exchange membrane AMVN (SELEMION™, ACG Engineering, Japan). All electrochemical experiments were conducted using a calibrated Gamry potentiostat (Gamry 600+ or Gamry 3000). A 3-electrode system was used in all electrochemical experiments, consisting of glassy carbon disks (Goodfellow, ⌀15 mm x 1 mm thick) as the working electrode. A leakless Ag/AgCl electrode (eDAQ) was used as the reference, while a graphite rod (TedPella, Spec-pure, ⌀1/8" × 20 cm long) was used as the counter electrode.

Electrocatalysis was conducted under a constant CO_2 flow rate controlled via an MFC at 20 sccm in both the anodic and cathodic compartments. The electrolyte resistance was measured three times prior to each chronoamperometry run using high-frequency electrochemical impedance spectroscopy, and the average value was used for iR compensation via positive feedback correction (85%). Chronoamperometry was carried out for 100 min. All potentials reported in this thesis are with respect to the RHE, unless stated otherwise.

The CO_2 reduction catalytic performance was assessed across various Cu-Ag ratios to identify the optimal composition under four different potential ranges: -1.0, -1.2, -1.4, and -1.6 V vs. RHE. All experiments were conducted in triplicate, and the results are presented as average values with corresponding error bars in all figures, along with standard deviations for the recorded values. The catalytic performance of the glassy carbon disks was also evaluated (**Fig S1a**), with predominant hydrogen selectivity. High-purity metallic Cu disks (99.999%) were assessed for their catalytic performance towards CO_2 in a custom-made electrocatalytic cell (**Fig S1b**), and the results closely matched those reported in the literature [11]. Additional CO_2RR product evaluation methods are described in **Supporting Information Section 1**.

4.5. Electrochemical Characterisation: Electrochemically Active Surface Area (ECSA), Electrochemical Impedance Spectroscopy (EIS) and Modified Pulse Voltammetry (mPV)

All the electrochemical characterisations were carried out in an open PTFE cell. A pre-reduction step was performed at -1.2 V vs. RHE for 10 mins before electrochemical characterisation methods to reflect CO_2RR condition.

Cyclic voltammetry (CV) measurements were conducted in 1 M $KHCO_3$ to improve the signals. CV scans were performed around the non-faradaic region near open circuit potential (OCP) between -0.6 V and -0.7 V vs. Ag/AgCl (equivalent to 0.0 to +0.1 V vs. RHE, **Fig S5a**). CV scans were performed at 14 different scan rates within the capacitive regions, ranging from 20 mV s^{-1} to 150 mV s^{-1}, with each subsequent scan rate increasing by 10 mV s^{-1}. Each scan rate was repeated three times, with only the 3rd scan used for data

View Article Online
DOI: 10.1039/D6TA02615J

analysis. The exposed geometric area of the working electrode is 1.327 cm^2 and was calculated by subtracting the geometric surface area of the glassy carbon disk from that of the O-ring. The ECSA of each catalyst was determined based on their respective surface roughness factors, which correlate directly with the slope obtained from the linear relationship between current density and scan rates (**Fig S5b**), based on previous literature [67].

EIS measurements were performed in 1 M $KHCO_3$ to improve the signals. Prior to the experiment, all samples were pre-reduced via chronoamperometry at 1.8 V vs Ag/AgCl (-1.2 V vs RHE) to reflect CO_2RR condition. EIS measurements were conducted across a wide range of cathode potentials under CO_2RR conditions. EIS spectra were collected across 40 different potentials, ranging from -0.59 to -2.59 V vs. Ag/AgCl, in 0.05 V increments, with an oscillation applied to the AC voltage of ±10 mV rms. The spectra were collected from 0.2 Hz to 100,000 Hz at 10 points per decade (**Fig S6a-b**). Gamry Echem Analyst (v7.9.0) was used to fit all Nyquist plots using the modified Armstrong-Henderson circuit model (**Fig S6c**).

mPV experiments is performed in 0.1 M $KHCO_3$, the same condition as CO_2RR without significant signal disturbance. mPV was tested with square wave potential step, consisting of a fixed upper bound of 0 V vs. Ag/AgCl (near OCP) for 18 s, and increasingly cathodic lower bound voltages ranging from -0.5 V to -2.4 V vs. Ag/AgCl, incrementally decreased by 0.1 V at 18 s holding time, for a total of 41 steps, with a total duration of 738 s. The current response is recorded every 3 ms interval. The area under the anodic decay current response is integrated using scipy.intergrate.simps and fitted using scipy.optimize.curve_fit from t = 0 s to t = 2 s. The integrated current response is then plotted against ΔV, which is the difference between V_{anodic} and $V_{cathodic}$. An example plot of applied voltage and the corresponding current response is shown in **Fig S12a**. More details are available in the Supporting Information Section 6.

Unless stated otherwise, all potentials were converted into V vs RHE for data analysis, as described previously. All experiments were performed in triplicate, and the results are presented as averages with their standard errors.

4.6. Additional Characterisation Techniques

X-ray photoelectron spectroscopy (XPS) spectra were measured using a Kratos AXIS Supra+ spectrometer equipped with an Al Kα x-ray excitation source ($h\nu$ = 1486.7 eV). The spot size was determined to be 700 x 300 µm (slot mode). 50 scans were taken for Cu and Ag, while all other elements (O, N, C) were averaged over 20 scans without Ar sputtering. Data were collected at 160 eV pass energy with a step size of 1 eV for survey scans, and at 40 eV pass energy with a step size of 0.1 eV for narrow scans. Charge compensation was achieved using low-energy neutralisation electrons. Casa XPS version 2.3.24PR1.0 was used to analyse the valence states from the XPS spectra and to calculate the elemental composition from the peak area, Thermo Avantage v5.9928 software was used. XPS data and detailed XPS fitting analyses are described in **Supporting Information Section 8**.

Transmission Electron Microscopy (TEM) analysis was conducted on a Thermo Science Talos F200X G2 (S)TEM (Thermo Fisher Scientific), operating at an accelerating voltage of 200 kV. As-grown samples were directly deposited onto a 16-window Si grid (16 x 0.1 mm) coated with 30 nm SiN_x (silicon nitride) membrane. Post CO_2RR samples were obtained by mechanically transferring the films from glassy carbon

View Article Online
DOI: 10.1039/D6TA02615J

disks, resuspended in isopropanol, and then dripped onto holey carbon film on nickel 200 mesh (50 µm) TEM grids. Gatan DigitalMicrograph software was used for image and data analysis. Elemental composition and distribution mapping were obtained using TEM-integrated EDS.

Inductively coupled plasma optical emission spectroscopy (ICP-OES) was performed on catholyte before and after CO2RR using Avio 200 (PerkinElmer). Neat samples were analysed, with spectroscopy grade 0.1 M HNO_3 washing solution. More details and results are presented in **Supporting Information Section 9**.

Credit authorship contribution statement

Stefanos Agrotis: Conceptualization, Methodology, Validation, Investigation, Visualization, Formal analysis, Data curation, Writing – original draft, Writing – review & editing. **Ming Lin:** Investigation: TEM experiments, TEM data acquisition, and analysis. **Kallum H. Mehta:** Investigation: catalysis, Writing – review & editing. **Oliver S.J. Hagger:** Investigation, APPJ Methodology. **Riko I. Made:** Writing – review & editing, Supervision. **Ivan P. Parkin**: Supervision, Project administration, Funding acquisition **Daren J. Caruana:** Writing – review & editing, Supervision, Project administration, Funding acquisition, Conceptualization. **Albertus D. Handoko:** Writing – original draft, Writing – review & editing, Visualization, Supervision, Project administration, Funding acquisition, Formal analysis, Data curation, Conceptualization.

Declaration of competing interest

The authors declare the following financial interests/personal relationships which may be considered as potential competing interests: Daren J Caruana has a patent “PLASMA JET DEPOSITION PROCESS” pending to UCL Business Ltd.

Acknowledgments

The authors acknowledge funding support from A*STAR through The Accelerated Catalyst Development Platform (Grant Reference No.: A19E9a0103), Advanced Manufacturing and Engineering Programmatic Fund (Grant Reference No.: A1898b0043), and the HTCO Seed Funding (Grant Reference No.: C231218004). This research used the TEM resources and facilities at the A*STAR Institute of Materials Research and Engineering (A*STAR IMRE).

The authors acknowledge funding support from the EPSRC (Project number EP/T024836/1) and UCL Department of Chemistry.

SA acknowledges A*STAR Research Attachment Program (Award number: HQ/R25-ARAP210201).

The authors would also like to acknowledge Dr Debbie Seng Hwee Leng (A*STAR, IMRE) for performing the ex-situ XPS experiments. The authors also acknowledge Mr Ng Fu Song and Mr Ong Wai Chung for ICP-OES experiments.

View Article Online
DOI: 10.1039/D6TA02615J

References

1. Kesicki, F.; Yanagisawa, A., Modelling the potential for industrial energy efficiency in IEA's World Energy Outlook. *Energy Efficiency* **2015,** *8* (1), 155-169.
2. Hertzberg, M.; Schreuder, H., Role of atmospheric carbon dioxide in climate change. *Energy & Environment* **2016,** *27* (6-7), 785-797.
3. Nitopi, S.; Bertheussen, E.; Scott, S. B.; Liu, X.; Engstfeld, A. K.; Horch, S.; Seger, B.; Stephens, I. E. L.; Chan, K.; Hahn, C.; Nørskov, J. K.; Jaramillo, T. F.; Chorkendorff, I., Progress and Perspectives of Electrochemical CO_2 Reduction on Copper in Aqueous Electrolyte. *Chem. Rev.* **2019,** *119* (12), 7610-7672.
4. Handoko, A. D.; Wei, F.; Jenndy; Yeo, B. S.; Seh, Z. W., Understanding heterogeneous electrocatalytic carbon dioxide reduction through operando techniques. *Nat. Catal.* **2018,** *1* (12), 922-934.
5. Gotz, M.; Lefebvre, J.; Mors, F.; Koch, A. M.; Graf, F.; Bajohr, S.; Reimert, R.; Kolb, T., Renewable Power-to-Gas: A technological and economic review. *Renewable Energy* **2016,** *85*, 1371-1390.
6. Smith, B. L.; Woodhouse, M.; Horowitz, K. A. W.; Silverman, T. J.; Zuboy, J.; Margolis, R. M. *Photovoltaic (PV) Module Technologies: 2020 Benchmark Costs and Technology Evolution Framework Results*; National Renewable Energy Laboratory (NREL): Golden, CO (United States), 01, 2021.
7. Wiser, R. H.; Bolinger, M.; Hoen, B.; Millstein, D.; Rand, J.; Barbose, G. L.; Darghouth, N. R.; Gorman, W.; Jeong, S.; Mills, A. D.; Paulos, B. *Wind Energy Technology Data Update: 2020 Edition*; Energy Markets and Planning Department, Lawrence Berkeley National Laboratory: Berkeley, CA, USA, 2020.
8. Jouny, M.; Luc, W.; Jiao, F., General Techno-Economic Analysis of CO_2 Electrolysis Systems. *Ind. Eng. Chem. Res.* **2018,** *57* (6), 2165-2177.
9. Handoko, A. D.; Khoo, H. H.; Halim, I.; Murugappan, K., Feasibility of CO_2 Capture and Utilization: From the LCA Perspective. In *Life Cycle Assessment*, Khoo, H. H.; Tan, R. B. H., Eds. World Scientific Publishing Co. Pte. Ltd.: Singapore, 2022; pp 39-53.
10. Hori, Y.; Wakebe, H.; Tsukamoto, T.; Koga, O., Electrocatalytic process of CO selectivity in electrochemical reduction of CO_2 at metal electrodes in aqueous media. *Electrochim. Acta* **1994,** *39* (11–12), 1833-1839.
11. Kuhl, K. P.; Cave, E. R.; Abram, D. N.; Jaramillo, T. F., New insights into the electrochemical reduction of carbon dioxide on metallic copper surfaces. *Energy Environ. Sci.* **2012,** *5* (5), 7050-7059.
12. Salehi-Khojin, A.; Jhong, H.-R. M.; Rosen, B. A.; Zhu, W.; Ma, S.; Kenis, P. J. A.; Masel, R. I., Nanoparticle Silver Catalysts That Show Enhanced Activity for Carbon Dioxide Electrolysis. *J. Phys. Chem. C* **2013,** *117* (4), 1627-1632.
13. Ting, L. R. L.; Piqué, O.; Lim, S. Y.; Tanhaei, M.; Calle-Vallejo, F.; Yeo, B. S., Enhancing CO_2 Electroreduction to Ethanol on Copper–Silver Composites by Opening an Alternative Catalytic Pathway. *ACS Catal.* **2020,** *10* (7), 4059-4069.
14. Qi, K.; Zhang, Y.; Onofrio, N.; Petit, E.; Cui, X.; Ma, J.; Fan, J.; Wu, H.; Wang, W.; Li, J.; Liu, J.; Zhang, Y.; Wang, Y.; Jia, G.; Wu, J.; Lajaunie, L.; Salameh, C.; Voiry, D., Unlocking direct CO_2 electrolysis to C_3 products via electrolyte supersaturation. *Nat. Catal.* **2023,** *6* (4), 319-331.
15. Gao, J.; Zhang, H.; Guo, X.; Luo, J.; Zakeeruddin, S. M.; Ren, D.; Grätzel, M., Selective C–C Coupling in Carbon Dioxide Electroreduction via Efficient Spillover of Intermediates As Supported by Operando Raman Spectroscopy. *J. Am. Chem. Soc.* **2019,** *141* (47), 18704-18714.
16. Herzog, A.; Bergmann, A.; Jeon, H. S.; Timoshenko, J.; Kühl, S.; Rettenmaier, C.; Lopez Luna, M.; Haase, F. T.; Roldan Cuenya, B., Operando Investigation of Ag-Decorated Cu_2O Nanocube Catalysts with Enhanced CO_2 Electroreduction toward Liquid Products. *Angew. Chem. Int. Ed.* **2021,** *60* (13), 7426-7435.

View Article Online
DOI: 10.1039/D6TA02615J

17. Clark, E. L.; Hahn, C.; Jaramillo, T. F.; Bell, A. T., Electrochemical CO_2 Reduction over Compressively Strained CuAg Surface Alloys with Enhanced Multi-Carbon Oxygenate Selectivity. *J. Am. Chem. Soc.* **2017,** *139* (44), 15848-15857.

18. Frisch, M. L.; Wu, L.; Atlan, C.; Ren, Z.; Han, M.; Tucoulou, R.; Liang, L.; Lu, J.; Guo, A.; Nong, H. N.; Arinchtein, A.; Sprung, M.; Villanova, J.; Richard, M.-I.; Strasser, P., Unraveling the synergistic effects of Cu-Ag tandem catalysts during electrochemical CO_2 reduction using nanofocused X-ray probes. *Nat. Commun.* **2023,** *14* (1), 7833.

19. Balakrishna, S. S.; Mallik, A. K., Synthesis of azeotropic and two terminal solid solution type binary diagrams. *Calphad* **1979,** *3* (2), 109-118.

20. Bhat, M. K.; Sukumar, P. T.; Langenohl, L.; Best, J. P.; Dehm, G., Role of Ag segregation on microscale strengthening and slip transmission in an asymmetric Σ5 copper grain boundary. *Acta Mater.* **2023,** *255*, 119081.

21. Sansoz, F.; Ke, X., Hall–Petch strengthening limit through partially active segregation in nanocrystalline Ag-Cu alloys. *Acta Mater.* **2022,** *225*, 117560.

22. Kamat, G. A.; Yan, C.; Osowiecki, W. T.; Moreno-Hernandez, I. A.; Ledendecker, M.; Alivisatos, A. P., Self-Limiting Shell Formation in Cu@Ag Core–Shell Nanocrystals during Galvanic Replacement. *J. Phys. Chem. Lett.* **2020,** *11* (13), 5318-5323.

23. Zhang, J.; Shao, Q.; Wang, P.; Guo, J.; Huang, X., Catalytic Hydrogen Production by Janus CuAg Nanostructures. *ChemNanoMat* **2018,** *4* (5), 477-481.

24. Chen, P.-C.; Gao, M.; Mccandler, C. A.; Song, C.; Jin, J.; Yang, Y.; Maulana, A. L.; Persson, K. A.; Yang, P., Complete miscibility of immiscible elements at the nanometre scale. *Nat. Nanotechnol.* **2024,** *19* (6), 775-781.

25. Sang, J.-L.; Zhang, S.-D.; Liu, Q.; Geioushy, R. A.; Mahmoud, T.; Zhang, Y.; Liu, M., Liquid-Liquid Interface -Driven Reconstruction of CuAg Nanocomposites for Selective CO_2 to C_2H_4 Electroreduction. *Small* **2025**, e08803.

26. Kim, I.; Lee, G.-B.; Kim, S.; Jung, H. D.; Kim, J.-Y.; Lee, T.; Choi, H.; Jo, J.; Kang, G.; Oh, S.-H.; Kwon, W.; Hong, D.; Kim, H. G.; Lee, Y.; Kim, U.; Kim, H.; Kim, M.; Back, S.; Park, J.; Joo, Y.-C.; Nam, D.-H., Unveiling the reconstruction of copper bimetallic catalysts during CO_2 electroreduction. *Nat. Catal.* **2025,** *8* (7), 697-713.

27. Mu, S.; Lu, H.; Wu, Q.; Li, L.; Zhao, R.; Long, C.; Cui, C., Hydroxyl radicals dominate reoxidation of oxide-derived Cu in electrochemical CO_2 reduction. *Nat. Commun.* **2022,** *13* (1), 3694.

28. Ma, Y.; Yu, J.; Sun, M.; Chen, B.; Zhou, X.; Ye, C.; Guan, Z.; Guo, W.; Wang, G.; Lu, S.; Xia, D.; Wang, Y.; He, Z.; Zheng, L.; Yun, Q.; Wang, L.; Zhou, J.; Lu, P.; Yin, J.; Zhao, Y.; Luo, Z.; Zhai, L.; Liao, L.; Zhu, Z.; Ye, R.; Chen, Y.; Lu, Y.; Xi, S.; Huang, B.; Lee, C. S.; Fan, Z., Confined Growth of Silver–Copper Janus Nanostructures with {100} Facets for Highly Selective Tandem Electrocatalytic Carbon Dioxide Reduction. *Adv. Mater.* **2022,** *34* (19), 2110607.

29. Yu, Y.; Wang, D.; Hong, Y.; Zhang, T.; Liu, C.; Chen, J.; Qin, G.; Li, S., Bulk-immiscible CuAg alloy nanorods prepared by phase transition from oxides for electrochemical CO_2 reduction. *Chem. Commun.* **2022,** *58* (79), 11163-11166.

30. Wang, D.; Jung, H. D.; Liu, S.; Chen, J.; Yang, H.; He, Q.; Xi, S.; Back, S.; Wang, L., Revealing the structural evolution of CuAg composites during electrochemical carbon monoxide reduction. *Nat. Commun.* **2024,** *15* (1), 4692.

31. Dai, H.; Dimitriadou, S.; Sankara Rama Krishnan, P. S.; Handoko, A. D.; Recatala-Gomez, J.; Wang, Y.; Repaka, D. V. M.; Thway, M.; Zhang, C.; Duchamp, M.; Hippalgaonkar, K., Sub-10 nm Mixing and Alloying of Cu-Ag and Cu-Ni via Accelerated Solid Diffusion. *ACS Appl. Mater. Interfaces* **2023,** *15* (23), 28398-28409.

32. Lockwood Estrin, F.; Hagger, O. S. J.; Sener, M. E.; Caruana, D. J., Metal Painting by Plasma Jet. *Adv. Mater. Interfaces* **2024,** *11* (25), 2400256.

View Article Online
DOI: 10.1039/D6TA02615J

33. Hagger, O. S. J.; Sener, M. E.; Khan, I.; Estrin, F. L.; Agrotis, S.; Handoko, A. D.; Parkin, I. P.; Caruana, D. J., Rapid single step atmospheric pressure plasma jet deposition of a SERS active surface. *Mater. Adv.* **2023,** *4* (15), 3239-3245.

34. Hagger, O. S. J.; Parkes, M. A.; Lockwood Estrin, F.; Agrotis, S.; Parkin, I. P.; Handoko, A. D.; Caruana, D. J., Additive metal printing on multi materials using an atmospheric pressure plasma jet on a 5-Axis platform. *Mater. Des.* **2025,** *251*, 113681.

35. Agrotis, S.; Emre Sener, M.; Hagger, O. S. J.; Handoko, A. D.; Caruana, D. J., One-Step synthesis of nanosized Cu-Ag films using atmospheric pressure plasma jet. *Appl. Mater. Today* **2024,** *39*, 102286.

36. Handoko, A. D.; Ong, C. W.; Huang, Y.; Lee, Z. G.; Lin, L.; Panetti, G. B.; Yeo, B. S., Mechanistic Insights into the Selective Electroreduction of Carbon Dioxide to Ethylene on Cu_2O-Derived Copper Catalysts. *J. Phys. Chem. C* **2016,** *120* (36), 20058-20067.

37. Cheng, T.; Xiao, H.; Goddard, W. A., Full atomistic reaction mechanism with kinetics for CO reduction on Cu(100) from ab initio molecular dynamics free-energy calculations at 298 K. *Proc. Natl. Acad. Sci. U. S. A.* **2017,** *114* (8), 1795-1800.

38. Kortlever, R.; Shen, J.; Schouten, K. J. P.; Calle-Vallejo, F.; Koper, M. T. M., Catalysts and Reaction Pathways for the Electrochemical Reduction of Carbon Dioxide. *J. Phys. Chem. Lett.* **2015,** *6* (20), 4073–4082.

39. Zhang, J.; Zeng, G.; Zhu, S.; Tao, H.; Pan, Y.; Lai, W.; Bao, J.; Lian, C.; Su, D.; Shao, M.; Huang, H., Steering CO_2 electroreduction pathway toward ethanol via surface-bounded hydroxyl species-induced noncovalent interaction. *Proc. Natl. Acad. Sci. U. S. A.* **2023,** *120* (11).

40. Lim, C. Y. J.; Yilmaz, M.; Arce-Ramos, J. M.; Handoko, A. D.; Teh, W. J.; Zheng, Y.; Khoo, Z. H. J.; Lin, M.; Isaacs, M.; Tam, T. L. D.; Bai, Y.; Ng, C. K.; Yeo, B. S.; Sankar, G.; Parkin, I. P.; Hippalgaonkar, K.; Sullivan, M. B.; Zhang, J.; Lim, Y.-F., Surface charge as activity descriptors for electrochemical CO_2 reduction to multi-carbon products on organic-functionalised Cu. *Nat. Commun.* **2023,** *14* (1), 335.

41. Liu, Z.; Song, L.; Lv, X.; Liu, M.; Wen, Q.; Qian, L.; Wang, H.; Wang, M.; Han, Q.; Zheng, G., Switching CO_2 Electroreduction toward Ethanol by Delocalization State-Tuned Bond Cleavage. *J. Am. Chem. Soc.* **2024,** *146* (20), 14260-14266.

42. Lin, Y.; Wang, T.; Zhang, L.; Zhang, G.; Li, L.; Chang, Q.; Pang, Z.; Gao, H.; Huang, K.; Zhang, P.; Zhao, Z.-J.; Pei, C.; Gong, J., Tunable CO2 electroreduction to ethanol and ethylene with controllable interfacial wettability. *Nat. Commun.* **2023,** *14* (1).

43. Tang, H.; Liu, Y.; Zhou, Y.; Qian, Y.; Lin, B.-L., Boosting the Electroreduction of CO2 to Ethanol via the Synergistic Effect of Cu–Ag Bimetallic Catalysts. *ACS Appl. Energy Mater.* **2022,** *5* (11), 14045-14052.

44. Wang, P.; Yang, H.; Tang, C.; Wu, Y.; Zheng, Y.; Cheng, T.; Davey, K.; Huang, X.; Qiao, S.-Z., Boosting electrocatalytic CO2–to–ethanol production via asymmetric C–C coupling. *Nat. Commun.* **2022,** *13* (1), 3754.

45. Gao, X.; Jiang, Y.; Liu, J.; Shi, G.; Yang, C.; Xu, Q.; Yun, Y.; Shen, Y.; Chang, M.; Zhu, C.; Lu, T.; Wang, Y.; Du, G.; Li, S.; Dai, S.; Zhang, L., Intermediate-regulated dynamic restructuring at Ag-Cu biphasic interface enables selective CO_2 electroreduction to C_{2+} fuels. *Nat. Commun.* **2024,** *15* (1), 10331.

46. Mavrikakis, M.; Hammer, B.; Nørskov, J. K., Effect of Strain on the Reactivity of Metal Surfaces. *Phys. Rev. Lett.* **1998,** *81* (13), 2819-2822.

47. Bruggeman, P. J.; Iza, F.; Brandenburg, R., Foundations of atmospheric pressure non-equilibrium plasmas. *Plasma Sources Sci. Technol.* **2017,** *26* (12), 123002.

48. Maguire, P. D.; Mahony, C. M. O.; Kelsey, C. P.; Bingham, A. J.; Montgomery, E. P.; Bennet, E. D.; Potts, H. E.; Rutherford, D. C. E.; McDowell, D. A.; Diver, D. A.; Mariotti, D., Controlled microdroplet transport in an atmospheric pressure microplasma. *Appl. Phys. Lett.* **2015,** *106* (22).

49. Maguire, P.; Rutherford, D.; Macias-Montero, M.; Mahony, C.; Kelsey, C.; Tweedie, M.; Pérez-Martin, F.; McQuaid, H.; Diver, D.; Mariotti, D., Continuous In-Flight Synthesis for On-Demand Delivery of Ligand-Free Colloidal Gold Nanoparticles. *Nano Lett.* **2017,** *17* (3), 1336-1343.

View Article Online
DOI: 10.1039/D6TA02615J

50. Langlois, C.; Li, Z. L.; Yuan, J.; Alloyeau, D.; Nelayah, J.; Bochicchio, D.; Ferrando, R.; Ricolleau, C., Transition from core–shell to Janus chemical configuration for bimetallic nanoparticles. *Nanoscale* **2012,** *4* (11), 3381.

51. Weng, W.-L.; Hsu, C.-Y.; Lee, J.-S.; Fan, H.-H.; Liao, C.-N., Twin-mediated epitaxial growth of highly lattice-mismatched Cu/Ag core–shell nanowires. *Nanoscale* **2018,** *10* (21), 9862-9866.

52. Kirfel, A.; Eichhorn, K., Accurate structure analysis with synchrotron radiation. The electron density in Al_2O_3 and Cu_2O. *Acta Crystallogr. A* **1990,** *46* (4), 271-284.

53. Wyckoff, R. W. G., *Crystal structures*. Interscience Publishers: New York, 1963; Vol. 1.

54. Viyannalage, L. T.; Vasilic, R.; Dimitrov, N., Epitaxial Growth of Cu on Au(111) and Ag(111) by Surface Limited Redox ReplacementAn Electrochemical and STM Study. *J. Phys. Chem. C* **2007,** *111* (10), 4036-4041.

55. Ren, D.; Deng, Y.; Handoko, A. D.; Chen, C. S.; Malkhandi, S.; Yeo, B. S., Selective Electrochemical Reduction of Carbon Dioxide to Ethylene and Ethanol on Copper(I) Oxide Catalysts. *ACS Catal.* **2015,** *5* (5), 2814-2821.

56. Biesinger, M. C., Advanced analysis of copper X-ray photoelectron spectra. *Surf. Interface Anal.* **2017,** *49* (13), 1325-1334.

57. Tomc, B.; Bele, M.; Plut, M.; Kostelec, M.; Popović, S.; Nazrulla, M. A.; Ruiz-Zepeda, F.; Kamšek, A. R.; Šala, M.; Elbataioui, A.; Rafailović, L. D.; Pissolitto, Y. B.; Trivinho-Strixino, F.; Stępniowski, W. J.; Suhadolnik, L.; Hodnik, N., Recognizing the Universality of Copper Reconstruction Via Dissolution–Redeposition at the Onset of CO_2 Reduction. *J. Phys. Chem. Lett.* **2025,** *16* (36), 9553-9560.

58. Anantharaj, S.; Noda, S., Appropriate Use of Electrochemical Impedance Spectroscopy in Water Splitting Electrocatalysis. *ChemElectroChem* **2020,** *7* (10), 2297-2308.

59. Armstrong, R. D.; Henderson, M., Impedance plane display of a reaction with an adsorbed intermediate. *J. Electroanal. Chem. Interfacial Electrochem.* **1972,** *39* (1), 81-90.

60. Harrington, D. A.; Conway, B. E., ac Impedance of Faradaic reactions involving electrosorbed intermediates—I. Kinetic theory. *Electrochim. Acta* **1987,** *32* (12), 1703-1712.

61. Huang, Y.; Handoko, A. D.; Hirunsit, P.; Yeo, B. S., Electrochemical Reduction of CO_2 Using Copper Single-Crystal Surfaces: Effects of CO* Coverage on the Selective Formation of Ethylene. *ACS Catal.* **2017,** *7* (3), 1749-1756.

62. Tezsevin, I.; van de Sanden, M. C. M.; Er, S., Surface charging activated mechanism change: A computational study of O, CO, and CO_2 interactions on Ag electrodes. *J. Energy Chem.* **2020,** *50*, 307-313.

63. Kenty, J. L.; Hirth, J. P., Epitaxy and heterogeneous nucleation theory. *Surf. Sci.* **1969,** *15* (3), 403-424.

64. Lei, Q.; Huang, L.; Yin, J.; Davaasuren, B.; Yuan, Y.; Dong, X.; Wu, Z.-P.; Wang, X.; Yao, K. X.; Lu, X.; Han, Y., Structural evolution and strain generation of derived-Cu catalysts during CO_2 electroreduction. *Nat. Commun.* **2022,** *13* (1), 4857.

65. Bogatyrenko, S. I.; Kryshtal, A. P.; Kruk, A., Effect of Size on the Formation of Solid Solutions in Ag–Cu Nanoparticles. *J. Phys. Chem. C* **2023,** *127* (5), 2569-2580.

66. Montoya, J. H.; Peterson, A. A.; Nørskov, J. K., Insights into C-C Coupling in CO_2 Electroreduction on Copper Electrodes. *ChemCatChem* **2013,** *5* (3), 737-742.

67. Li, C. W.; Ciston, J.; Kanan, M. W., Electroreduction of carbon monoxide to liquid fuel on oxide-derived nanocrystalline copper. *Nature* **2014,** *508* (7497), 504-507.

View Article Online
DOI: 10.1039/D6TA02615J

In addition to the main text, additional supporting data has been provided as part of the Supplementary information: CO_2RR product evaluation methods, CO_2 reduction performance of baseline on Cu and blank glassy carbon, Additional electron microscopy analyses. Electrochemical active surface area (ECSA) estimation, Electrochemical impedance spectroscopy (EIS) measurements and fitting, Modified pulse voltammetry (mPV) measurements, Surface Cu fraction post CO2RR correlation to C2+ selectivity, XPS data and analysis